2011

Investigations of Anatomical Connectivity in the Internal Capsule of Macaques with Diffusion Magnetic Resonance Imaging

Kyle Andrew ignatius Taljan
Cleveland State University

INVESTIGATIONS OF ANATOMICAL CONNECTIVITY IN THE INTERNAL CAPSULE OF MACAQUES WITH DIFFUSION MAGNETIC RESONANCE IMAGING

KYLE ANDREW IGNATIUS TALJAN

Bachelor of Arts in Physics

Oberlin College

May, 2009

Submitted in partial fulfillment of requirements for the degree

MASTER OF SCIENCE IN BIOMEDICAL ENGINEERING

at

CLEVELAND STATE UNIVERSITY

July, 2011

This thesis has been approved

for the Department of Chemical and Biomedical Engineering

and the College of Graduate Studies by

_____

Thesis Committee Chairperson, **Cameron McIntyre, Ph.D.**

Department of Chemical and Biomedical Engineering

_____

Date

_____

Ken Sakaie, Ph.D.

Department of Chemical and Biomedical Engineering

_____

Date

_____

Nolan Holland, Ph.D.

Department of Chemical and Biomedical Engineering

_____

Date

I would like to dedicate this thesis to my parents whose hard work has sustained me, whose love has nurtured me, and whose example inspires me.

I would also like to dedicate this thesis to serendipity who intervened wonderfully in my life when I did not quite know where I was going.

INVESTIGATIONS OF ANATOMICAL CONNECTIVITY IN THE INTERNAL CAPSULE OF MACAQUES WITH DIFFUSION MAGNETIC RESONANCE IMAGING

KYLE ANDREW IGNATIUS TALJAN

ABSTRACT

Understanding anatomical connectivity is crucial for improving outcomes of deep brain stimulation surgery. Tractography is a promising method for noninvasively investigating anatomical connectivity, but connections between subcortical regions have not been closely examined by this method. As many connections to subcortical regions converge at the internal capsule (IC), we investigate the connectivity through the IC to three subcortical nuclei (caudate, lentiform nucleus, and thalamus) in 6 macaques. We show that a statistical correction for a known distance-related artifact in tractography results in large changes in connectivity patterns. Our results suggest that care should be taken in using tractography to assess anatomical connectivity between subcortical structures.

TABLE OF CONTENTS

Page

LIST OF TABLES

LIST OF FIGURES

CHAPTER I

INTRODUCTION

1.1 Deep Brain Stimulation

Deep brain stimulation (DBS) is a medical procedure in which an electrode is placed deep in the subcortical structures of the brain to deliver electrical impulses to the surrounding tissues. Conceptually, it is believed that DBS plays an analogous role to a pacemaker for the heart, limiting erratic firing between subcortical structures thereby allowing normal firing patterns to be reestablished. Currently, DBS is the gold standard treatment for severe refractory Parkinson's disease relieving a broad range of symptoms such as rigidity, bradykinesia, and tremor[1-4]. DBS has also been used for other motor degenerative conditions such as essential tremor and dystonia[5,6]. In addition, there is a great deal of research on expanding DBS to treat non-motor conditions such as epilepsy, obsessive-compulsive disorder, and severe depression[7-9]. Figure 1 shows a qualitative rendering of a typical DBS implant.

However, even in the case of Parkinson's disease there is a fundamental lack of understanding as to how DBS works[10]. Patients with similar clinical symptoms can undergo a DBS procedure with different results. One patient may experience a complete

reversal of symptoms regaining normal motor control, whereas another patient may experience some improvement in one symptom with an accompanying increase in secondary motor, cognitive, or emotional side effects[11].

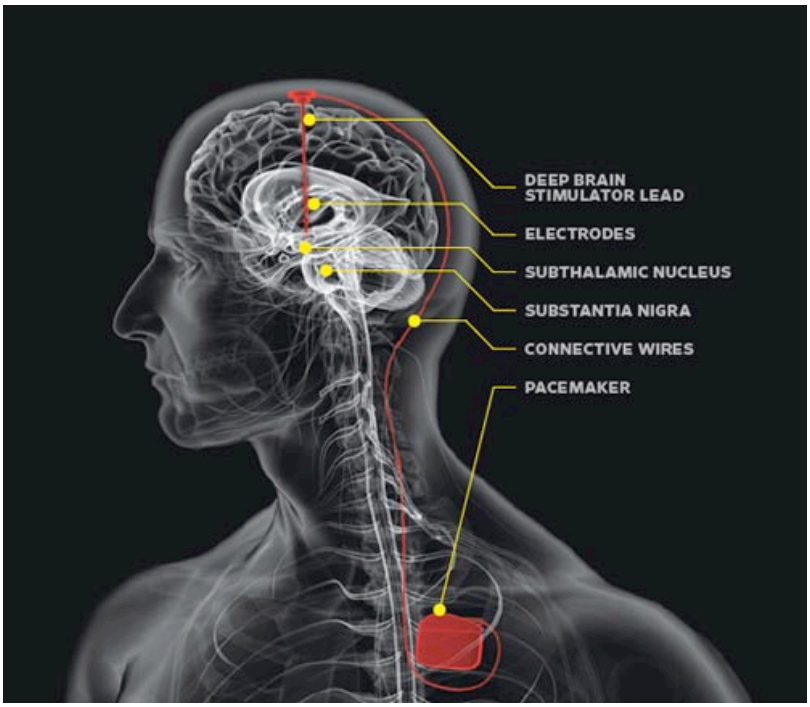

Figure 1. A typical deep brain stimulation implantation. The electrodes penetrate deep into the subcortical structures of the brain, and the connective wires are run under the skin to a pacemaker that is implanted in the chest[12].

There is hope that DBS performance can be improved by constructing accurate models of Parkinson's disease motor circuits[13]. However, the complex network architecture of the subcortical motor circuits presents a formidable challenge to modeling because it is not possible to discern direct cause and effect relationships. Each region in the motor circuit has many inputs and outputs so that stimulating the subthalamic nucleus does not just effect the thalamus, but also effects the putamen, globus pallidus, motor

cortex, etc. all of which are themselves interconnected. The result is that after years of DBS treatment for Parkinson's disease there are still multiple subcortical targets for stimulation and disagreement as to which targets are optimum[14,10].

In modeling the effects of DBS stimulation on the motor circuits a simple first step is to understand which regions are being directly stimulated. Much work has been done to calculate the volume of tissue activated around the electrode[15-17]. Knowing the volume of tissue activated we can identify areas correlated with negative or positive clinical outcomes. For example, the subthalamic nucleus, one of the most common targets for DBS in Parkinson's disease, is divided into motor and non-motor regions. A recent paper has shown that direct stimulation of non-motor regions is associated with an increase in negative side effects without an accompanying increase in positive outcomes[11].

Determining the volume of tissue activated is only the first step in understanding how DBS modulates the motor circuits affected in Parkinson's disease. The next step is to determine connections to the volume of tissue activated. By mapping the anatomical connections between the volume of tissue activated and other parts of the cortico-subcortical motor circuit we can begin to unravel cause and effect relationships in order to optimize electrode placement and stimulation parameters[10,13].

1.2 Diffusion MRI and Tractography

Tractography is the only currently available method for noninvasively investigating anatomical connections in the brain[18-20]. Diffusion magnetic resonance imaging (dMRI) serves as the foundation for tractography. dMRI is capable of measuring

the diffusion of water in the brain on the millimeter scale. It is known that cell membranes of neurons present a barrier to the free diffusion of water[21]. An oversimplified conclusion is that given the diffusion profile in a brain voxel whichever direction diffusion is greatest is the same direction as the principle fiber tracts. Tractography is the process of implementing an algorithm to connect voxels based on the diffusion profiles and thereby create maps of anatomical connections. In order to put the tractography work performed here into context it is necessary to give a history and description of dMRI.

Diffusion is the random movement of molecules in a fluid due to thermal energy independent of bulk flow. The theoretical description of diffusion on which dMRI is based was made by Einstein in 1905[22]. Torrey was the first to describe how the Bloch equations (the central equations in magnetic resonance imaging) change with the addition of diffusion[23]. In 1965 Stejskal and Tanner published the paper that is still the practical foundation of dMRI today[24]. In this paper they derived the Stejskal-Tanner equation describing how scan parameters affect signal in diffusion scans.

$$\frac{S}{S_0} = e^{-\gamma^2 G^2 \delta^2 (\Delta - \delta/3) D} = e^{-bD}$$

(1)

In (1) S is the diffusion signal, S_0 is the non-diffusion weighted signal, γ is the gyromagnetic ratio, G is the strength of the diffusion gradient, δ is the duration of the gradient, Δ is the time between gradients, and D is the diffusivity of the voxel. In discussing dMRI it is common to group all of the terms in the exponential together as a

single variable b. This b-value gives a measure of the amount of diffusion weighting. In practice to create a diffusion weighted image (DWI) we run a scan without any diffusion weighting (an S_0 image). Then, selecting a b-value we measure our signal S allowing us to solve for the diffusion constant D.

Figure 2 gives a qualitative explanation of how a diffusion weighted pulse sequence works. With no gradient the spins of hydrogen atoms process at the same rate in the constant B_0 field. The first magnetic field gradient causes a gradient in the rate of spin procession. When we apply the second, opposite gradient all spins should realign and process at the same rate. However if water has diffused in the direction of the gradient there will be signal loss due to the mixing of dephased spins. Large signal loss means a large amount of diffusion in the gradient direction, and little signal loss means relatively little diffusion. Diffusion perpendicular to gradient will result in no signal loss because all hydrogen atoms perpendicular to the gradient will be processing at the same rate. Consequently, each DWI image is dependent on the direction of the applied gradient. Changing the gradient direction or misaligning the patient in the scanner results in different images.

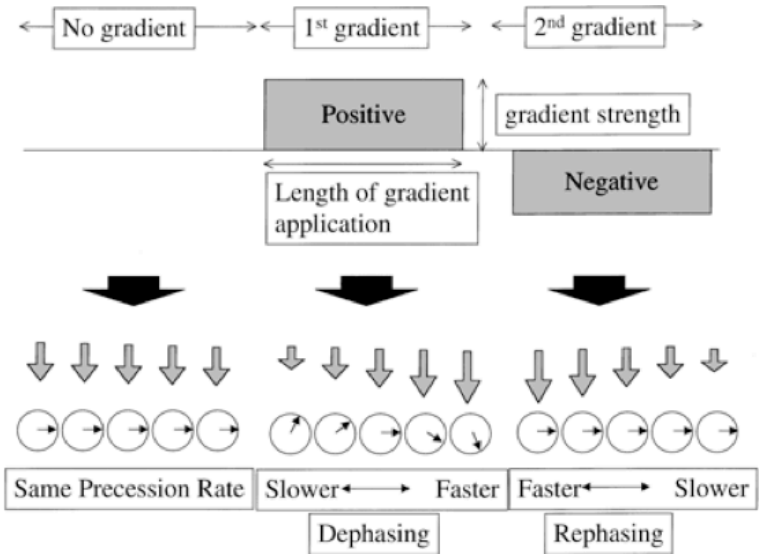

Figure 2. Description of the effect of diffusion weighting gradients. With no magnetic gradient the spins process at the same rate. The first gradient causes spins in the higher field to process faster than those in the lower field. If there is no diffusion along the direction of the diffusion weighting gradient then the spins should perfectly rephase after the second, opposite gradient. If there is diffusion along the gradient then there will be signal loss (taken from[25] figure 6).

The need for an objective, i.e. gradient independent, method of modeling diffusion culminated in 1994 with Peter Basser's implementation of the tensor model for diffusion[26]. Basser modeled diffusion in each voxel as a 3x3 positive, symmetric, semi-definite tensor describing how to estimate the diffusion tensor from a series of at least 6 different diffusion gradients using a least squares fitting algorithm[27]:

$$\mathbf{D}=\begin{bmatrix} d_{11} & d_{12} & d_{13} \\ d_{21} & d_{22} & d_{23} \\ d_{31} & d_{32} & d_{33} \end{bmatrix}$$

Diffusion tensors can be diagonalized into three eigenvalues and eigenvectors where the principle eigenvalue and eigenvector correspond to the direction of greatest diffusion for that voxel. The eigenvectors define the gradient independent coordinate system. The eigenvalues and eigenvectors can be visualized as a diffusion ellipsoid as seen in figure 3.

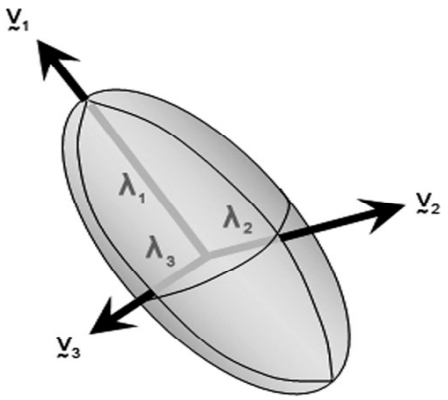

Figure 3. Visualization of a diffusion tensor. The direction of the largest eigenvalue, y_1, corresponds to the direction of greatest diffusion. All eigenvectors are orthogonal and define a gradient independent coordinate system for each voxel.

Fractional anisotropy (FA), an important invariant of the tensor model, measures how much the diffusion ellipsoid is pointed[28]. High FA voxels have ellipsoids shaped like

cigars and generally correspond to densely packed white matter tracts. Low FA ellipsoids are spherical and usually correspond to grey matter or voxels with a mix of different fiber directions.

Shortly after the advent of the diffusion tensor model, researchers began developing algorithms to plot tracks through regions of high FA. Early tractography algorithms would plot a streamline from a seed voxel by calculating the single most likely path through the diffusion data[29-31]. Qualitatively, the cigar-shaped ellipsoids in these high FA regions functioned like arrows where streamline algorithms found the most likely path connecting these arrows. The underlying assumption was that these streamlines through the diffusion data somehow mirrored the actual anatomical tracts of white matter in the brain.

The diffusion tensor model and streamline tractography have serious limitations. The fiber structure in the brain is intrinsically complex with many regions where white matter tracts assume complex geometries such as crossing or kissing[32]. The diffusion tensor model is unable to resolve crossing fibers because the tensor has only a single peak. An example where this single peak in inadequate is the case of two fibers crossing at an acute angle in a single voxel. The tensor will have its principle eigenvector pointing between the two fibers accurately capturing the anatomy of neither tract.

Streamline tractography does not account for the uncertainty in the fitting of the diffusion data[33]. This is a serious limitation given that streamline tractography plots only one fiber track per seed voxel and given that many fiber tracts pass through a single voxel in the actual brain. Figure 4 shows a comparison of the diffusion profile for the tensor model and persistent angular structure, a model that allows for multiple diffusion peaks.

There are numerous voxels with crossing fibers seen in the persistent angular structure reconstruction. These voxels with crossing fibers are inaccurately modeled as spheres in the tensor model.

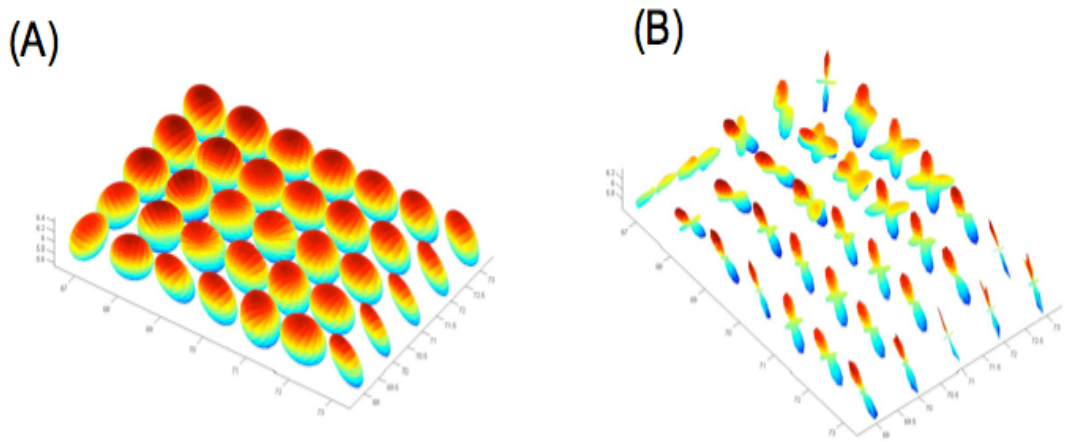

Figure 4. A comparison of the diffusion tensor model and persistent angular structure for the same section of the brain. (A) The diffusion tensor model is composed primarily of spherical diffusion profiles leading to the spurious conclusion that there are not tightly organized white matter fibers present. (B) Persistent angular structure is able to depict multiple diffusion peaks for each voxel revealing that the region is actually composed of well organized, crossing fibers.

Over the last decade many methods have been developed revamping the tensor model to allow for multiple diffusion peaks and exchanging deterministic tractography for probabilistic algorithms that plot numerous tracks from a single seed voxel[34-36]; however, it is unclear which of these methods may be optimum. The non-tensor models of diffusion often use functions such as high order spherical harmonics to capture

multiple diffusion peaks. Probabilistic algorithms calculate an uncertainty for each step along a track. This uncertainty in fiber direction in a voxel is used as the basis of a fibre orientation distribution (FOD). The FOD at each voxel is used as the sample distribution for determining each step as a track is plotted. The result is a large number tracks being generated for each voxel where the greater the uncertainty in the diffusion profile the greater the spread in tracks[37].

Recent studies using non-tensor models and probabilistic tractography have revealed striking results that seem to agree with past [18,20]. However, tractography is an indirect measure of anatomical connectivity. Great caution must be taken before interpreting tracks generated via tractography as representing actual white matter fascicles[38].

Due to the propagation of uncertainty in the fiber orientation probability density functions there is a known artifact in probabilistic tractography in which proximal regions are systematically more highly connected than distal regions[39,19]. For probabilistic algorithms even along well-organized, straight fiber tracts, voxels close to a seedpoint will have a higher percentage of tracks than voxels further from the seedpoint because of the propagation of uncertainty. The result is a 'flare' pattern of high track frequency in regions near the seedpoint where uncertainty is low and low track frequency further from the seed as uncertainty grows. Subcortical structures are particularly susceptible to this bias because of their proximity to each other. Correcting this bias may prove essential in establishing probabilistic tractography as a noninvasive tool for measuring anatomical connectivity, especially in the subcortical regions important to DBS. However, almost no work has been done to correct for uncertainty propagation in probabilistic tractography.

Recently, Morris et al. have introduced a statistical correction (the "Morris correction") to address this issue, but it has not been widely used[39].

1.3 Anatomy

The internal capsule (IC), a bundle of white matter fibers, is particularly important in DBS. The IC divides the thalamus and caudate from the lentiform nucleus running close to most of the important DBS targets including the subthalamic nucleus, globus pallidus interna, and thalamus[40]. Figure 5 below shows an axial view of the internal capsule along with the surrounding subcortical structures. The IC itself is the object of ongoing research as a potential target for DBS treatment for severe depression[41,8,14].

Given that the IC is highly connected to both subcortical and cortical structures it has the potential to spread stimuli far from the site of activation[41]. Such stimulus spread could be beneficial, allowing stimulation of a variety of target structures from one activation site. However, unintentional stimulation of the wrong structures could lead to side effects[42]. Of practical importance is that white matter requires lower stimulation thresholds than gray matter nuclei—a beneficial feature for DBS performance in general[11].

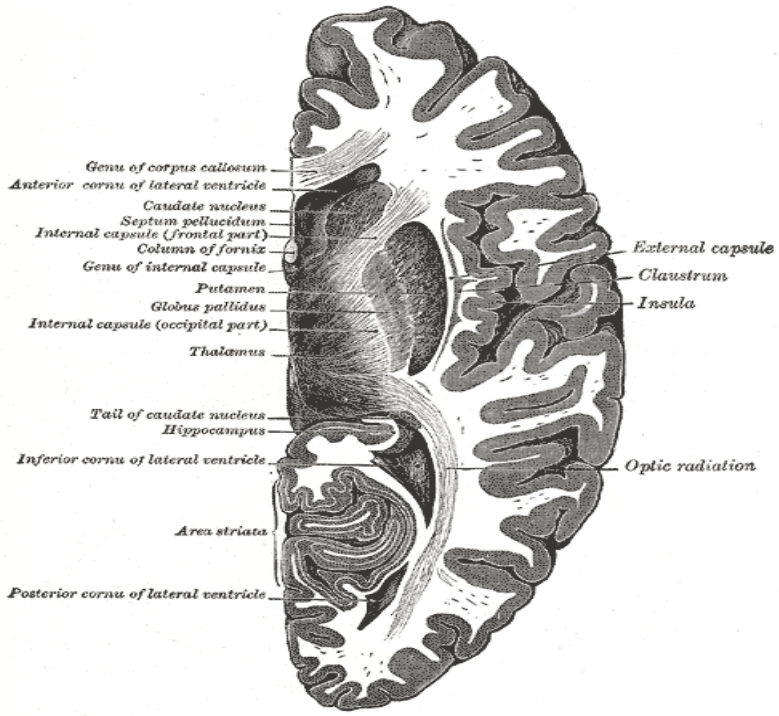

Figure 5. Drawing of axial slice of one hemisphere of a human brain showing the internal capsule and other important subcortical nuclei. The internal capsule is a white matter tract separating the caudate and thalamus from the lentiform nucleus[43].

1.4 Overview

In this work we use tractography to segment the IC in 6 macaques based on anatomical connectivity to three subcortical nuclei: the caudate, lentiform nucleus (LN), and thalamus. We perform segmentation with and without the Morris correction. The principal foci of this work are:

- Using tractography we demonstrate connection among deep brain structures correcting for the known distance bias. This is one of the few tractography studies of subcortical connections.
- We find that the Morris correction has a large impact on connectivity results.

Without the correction, the patterns of connectivity are largely governed by proximity. With the correction we find many examples in which proximity does not determine connectivity. In some studies the correction reveals areas of the IC with no significant connections to one or more target structures.

- We find that the caudate is most strongly and consistently connected to the anterior limb of the IC. The LN is most strongly and consistently connected to the lateral genu of the IC. The thalamus is most strongly and consistently connected to the medial genu of the IC.

CHAPTER II

METHODS

2.1 Imaging and Postprocessing

Six rhesus macaques (*macaca mulatta*) were scanned under a protocol approved by the Cleveland Clinic Institutional Animal Care and Use Committee. Animals were anesthetized with a propofol drip and held snugly on a Plexiglas board to minimize motion. High angular resolution diffusion imaging (HARDI)[32] (71 diffusion weighted image volumes with b=1000 sec/mm^2, 8 b=0 images) was performed at high spatial resolution (96x96mm FOV, 64x64 matrix, 1.5 mm slice thickness, yielding 1.5 x 1.5 x 1.5 mm voxels) with TR=2000 ms, TE=87 ms, NEX ranging from 23 to 36 (corresponding to acquisition time of 4-6 hours) on a Siemens 3 tesla Trio (Erlangen, Germany). Partial brain scans (14 or 15 1.5 mm thick slices) centered on the deep brain structures were performed to improve signal-to-noise ratio (SNR). The SNR was approximately 40 and 10 for the b=0 and diffusion-weighted images, respectively. Table 1 below gives the SNR for the internal capsule, caudate, LN, and thalamus for each of the six studies for the b=0 scans (i.e. the non-diffusion weighted scans). Table 2 shows the SNR for the diffusion weighted scans.

Study	Internal Capsule	Caudate	Lentiform Nucleus	Thalamus
1	30.1	37.1	26.8	33.6
2	29.4	35.4	28.3	29.4
3	34.0	54.4	37.4	34.6
4	30.3	39.7	30.3	30.2
5	45.5	53.6	43.8	48.1
6	55.5	65.6	52.1	59.0

Table 1. Signal to noise ratio for the non-diffusion weighted scans for each of the six studies.

Study	Internal Capsule	Caudate	Lentiform Nucleus	Thalamus
1	5.0	11.4	11.3	9.3
2	4.9	8.9	10.0	9.2
3	5.4	9.8	11.4	10.1
4	5.1	10.9	10.9	9.2
5	5.4	13.8	13.4	10.8
6	5.7	12.8	14.0	11.2

Table 2. Signal to noise ratio for the diffusion weighted scans for each of the six studies.

At each voxel, the diffusion tensor was calculated using a standard log-linear fit[27] and fractional anisotropy (FA) was calculated from the diffusion tensor[44]. The fiber orientation distribution (FOD) was calculated at each voxel using regularized spherical deconvolution[45,46]. The FOD was then used as the basis of probabilistic tractography.

2.2 Tractography

We assessed anatomical connectivity between the IC and 3 surrounding subcortical structures: caudate, lentiform nucleus (LN), and thalamus. For each study, caudate, LN, and thalamus ROIs were drawn by hand on coronal and axial FA images on the right side of the brain using the Saleem and Logothetis MRI histology atlas of the rhesus macaque as a reference[47]. We limited the IC at the posterior using a line between the posterior borders of thalamus and lentiform nucleus and at the anterior using a line between anterior borders of caudate and lentiform nucleus[48]. The medial and lateral borders of the IC were easy to distinguish because of the sharp contrast between the bright white matter of the IC and the dark surrounding gray matter. The superior and inferior borders were defined based on the boundaries of the caudate, LN, and thalamus in conjunction with the Saleem atlas. Figure 6 shows an example of a manual ROI for one study.

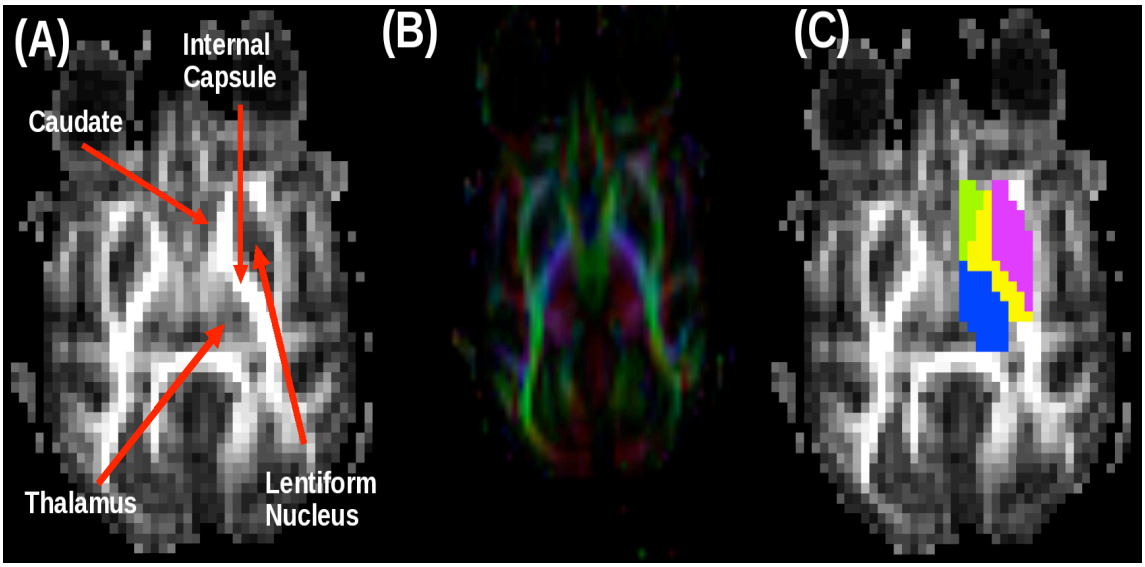

Figure 6. Example of manual ROIs drawn on an FA map. (A) the FA map with labeled arrows pointing to the IC, caudate, LN, and thalamus. (B) is the color FA image, and (C) shows the ROIs selected for this slice.

Probabilistic tractography was used to define anatomical connectivity between each voxel in the IC and the three subcortical structures of interest. We ran an in-house algorithm using a rejection sampling approach based on the FOD[45,49]. We generated 250 tracks per IC seed voxel with a step length of 1.125 mm and maximum bending angle of 90°. Tracks initiated in the seed region (IC) proceeded throughout the entire brain until the tracks left a mask defined using a robust range threshold on the b=0 image[50].

2.3 The Morris Correction

As the tractography algorithm is probabilistic, a given voxel in the IC typically exhibited connections to each nucleus. To correct for distance-related bias, we performed the correction developed by Morris[39]. The correction provides a framework for

determining whether connectivity between a seed voxel and a given target is statistically significant. The method has been shown to account for distance artifact in anatomical connectivity results. The key insight of the Morris correction is to compare track counts generated by probabilistic tractography to a null distribution, thus allowing the statistical comparison. In practice, the null distribution is simply achieved by repeating the tractography with an isotropic FOD. The null distribution therefore provides a map of connections due purely to chance instead of the directionality inferred from diffusion anisotropy.

2.4 Connection Profiles and Segmentation

To assess the impact of the Morris correction, we generated an anatomical connectivity profile of the IC to each subcortical nucleus and then performed a so-called "hard segmentation" of the IC[48]. The anatomical connectivity profiles were generated by superimposing the target ROIs on the whole brain tractography results seeded from each IC voxel and adding up the number of tracks that intersect that ROI. The hard segmentation classified each IC voxel according to which target had the highest number of connecting tracks. The connectivity profiles and the segmentation were performed with and without the Morris correction.

CHAPTER III

RESULTS

Figure 7 demonstrates the overall impact of the Morris correction. Connectivity through the IC from caudate is shown with and without the Morris correction. For comparison, the null distribution map is also shown. As the null distribution map does not include information from tissue microstructure, it primarily reflects the proximity between individual voxels of the IC and the caudate. The null distribution map and the connectivity map without the Morris correction demonstrate a high degree of similarity. After the correction, the connectivity profile is qualitatively different from the null distribution map.

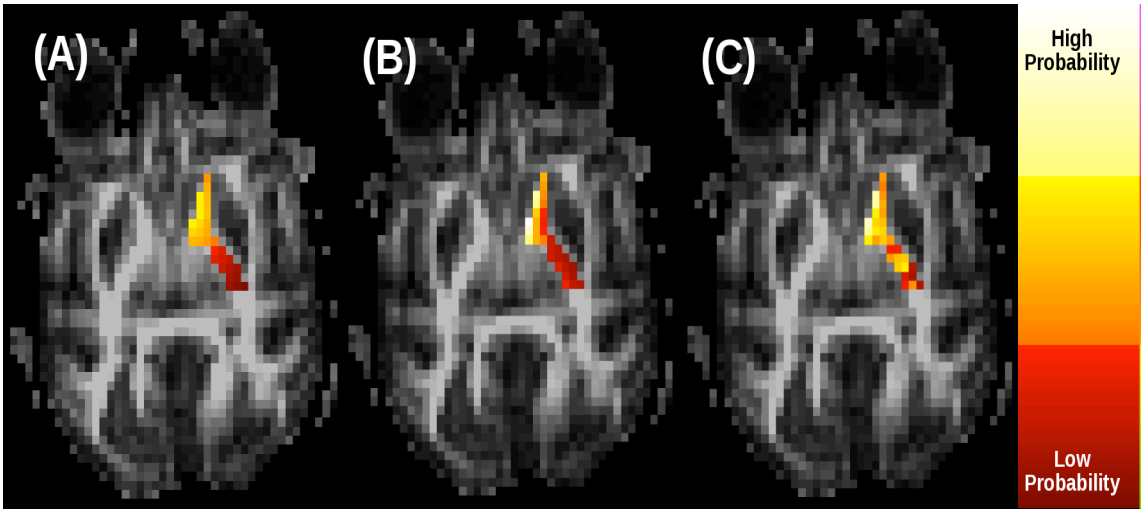

Figure 7. Overall impact of Morris correction on profile of connections from caudate

through the IC. (A) shows the null distribution map. (B) and (C) show connection profiles before and after the correction, respectively.

Figure 8 demonstrates the effect of the Morris correction on the anatomical connectivity profile. Before the correction, regions of IC close to the caudate are more connected than those further away – there are many connections from caudate running through the anterior limb of the IC, fewer connections between caudate and genu of IC, and fewer still from caudate running through the posterior limb of IC. The correction results in a large reorganization of the connection pattern. The anterior limb is still highly connected. However, a portion of the genu and posterior limb (both relatively far from the caudate) become highly connected after the correction. Some of the posterior limb remains weakly connected, showing that the impact of the filter is not uniform. Variability of connectivity is particularly high in the posterior limb of IC even after the correction.

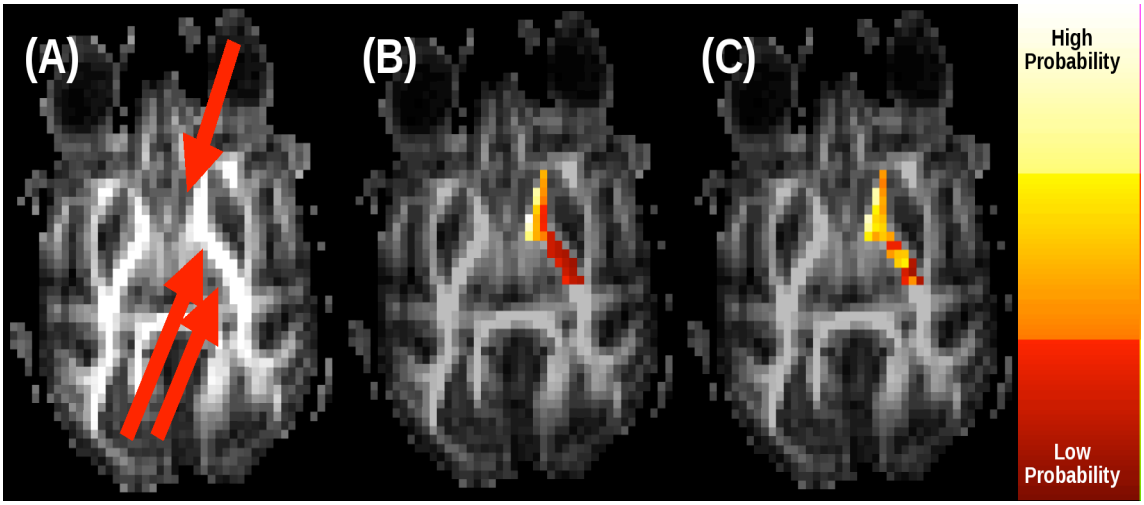

Figure 8. Effect of Morris correction on connectivity between IC and caudate. (A) Fractional anisotropy image indicating location of the caudate (single arrow) and IC

(double arrow). Connectivity (B) without and (C) with correction.

Figures 9 and 10 show reorganization of IC connections to the LN and thalamus due to the Morris correction. Without the correction, regions located closer to the LN or thalamus are systematically more connected than those further away. After the correction, lateral genu of IC shows high connectivity to the LN while medial genu of the IC show high connectivity to thalamus. These patterns are consistent among subjects.

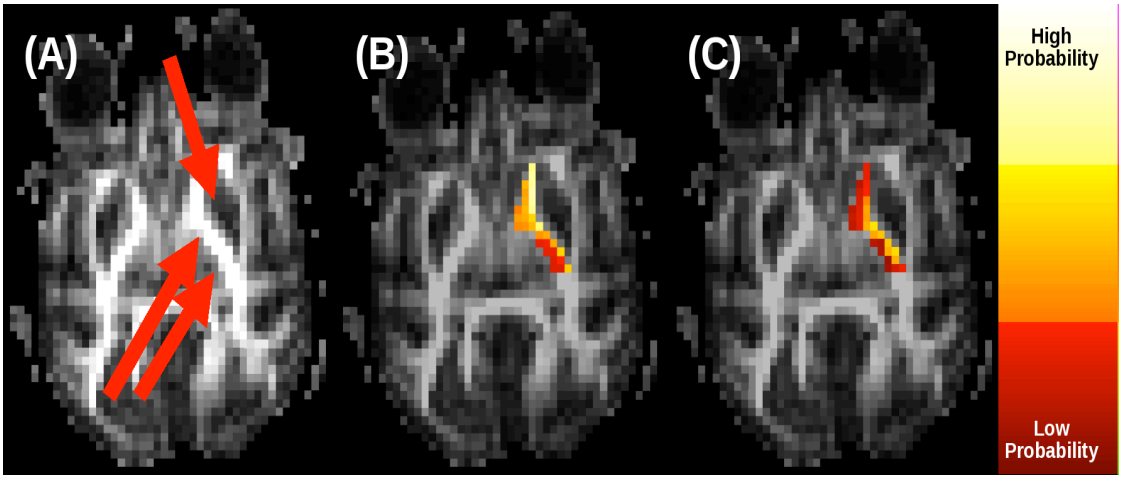

Figure 9. Effect of Morris correction on connectivity between the IC and LN. (A) Fractional anisotropy image, indicating location of the LN (single arrow) and IC (double arrow). Connectivity (B) without and (C) with correction.

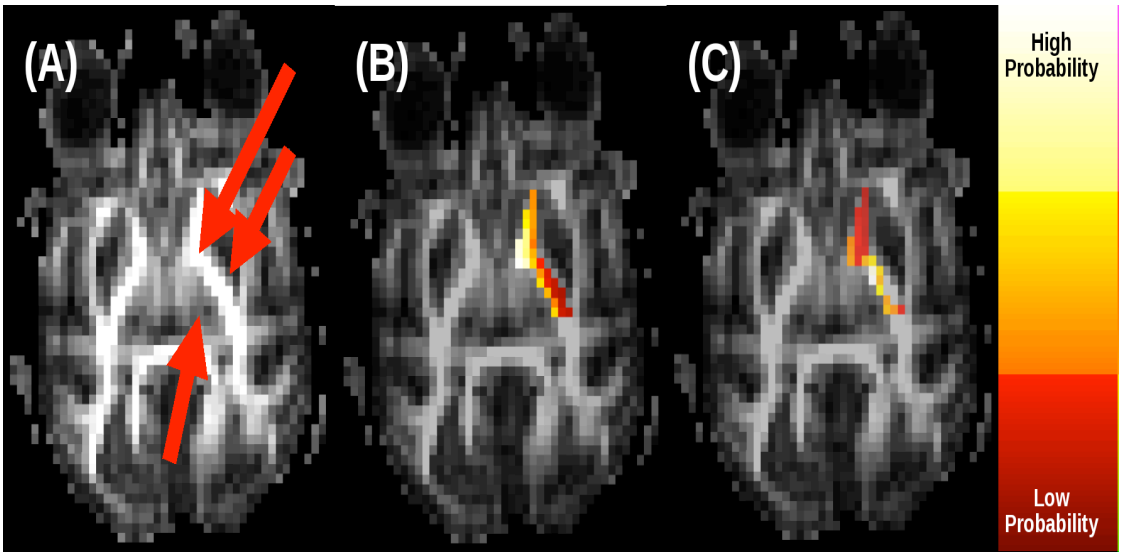

Figure 10. Effect of Morris correction on connectivity between the IC and thalamus. (A) Fractional anisotropy image indicating location of the thalamus (single arrow) and IC (double arrow). Connectivity (B) without and (C) with correction.

Figure 11 shows the connectivity profile after correction for each of the three targets across the 6 studies. Row A shows the connectivity profiles for the caudate, row B for the LN, and row C for the thalamus. We observe similar connection patterns to those mentioned above where caudate is most connected to anterior limb of IC, LN to lateral genu, and thalamus to medial genu. Significantly, with the correction we see that numerous regions across the different targets have no significant connections at all. Many voxels in the genu of the IC have no significant connections to the caudate (row A). Interestingly, there are still significant connections between the caudate and the distant posterior IC even in studies where voxels in the genu of the IC show no significant connection to the caudate. The LN shows least connection and occasional dropout of connection to posterior limb of IC and medial genu. The thalamus has highest connectivity throughout the entire IC with minimal number of insignificantly connected

voxels in the anterior limb and lateral genu.

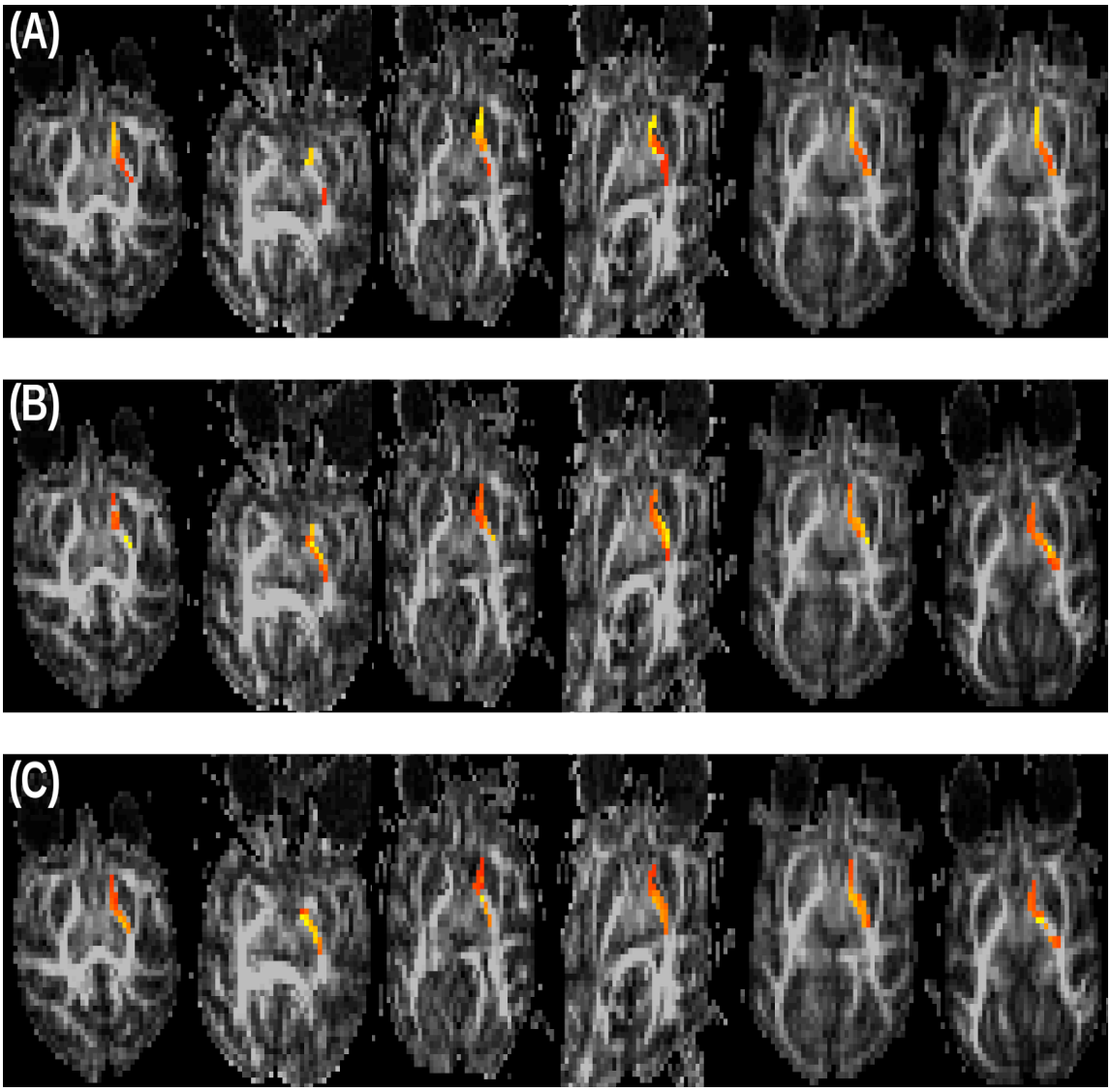

Figure 11. Connectivity maps after the Morris correction for all three structures across all 6 studies. The top row (A) shows connectivity profiles between IC and caudate, the middle row (B) profiles between IC and LN, and the bottom row (C) between IC and thalamus. Across the three structures we observe regions with no significant connections.

Hard segmentation provides a means for comparing connection differences among the three target structures. The statistical correction had a strong impact on hard

segmentation results as 23±6% of voxels change classification. However, there does not appear to be an obvious pattern to which regions change classification because of the correction. Figure 12 shows hard segmentation results for all six studies before (row A) and after (row B) the correction.

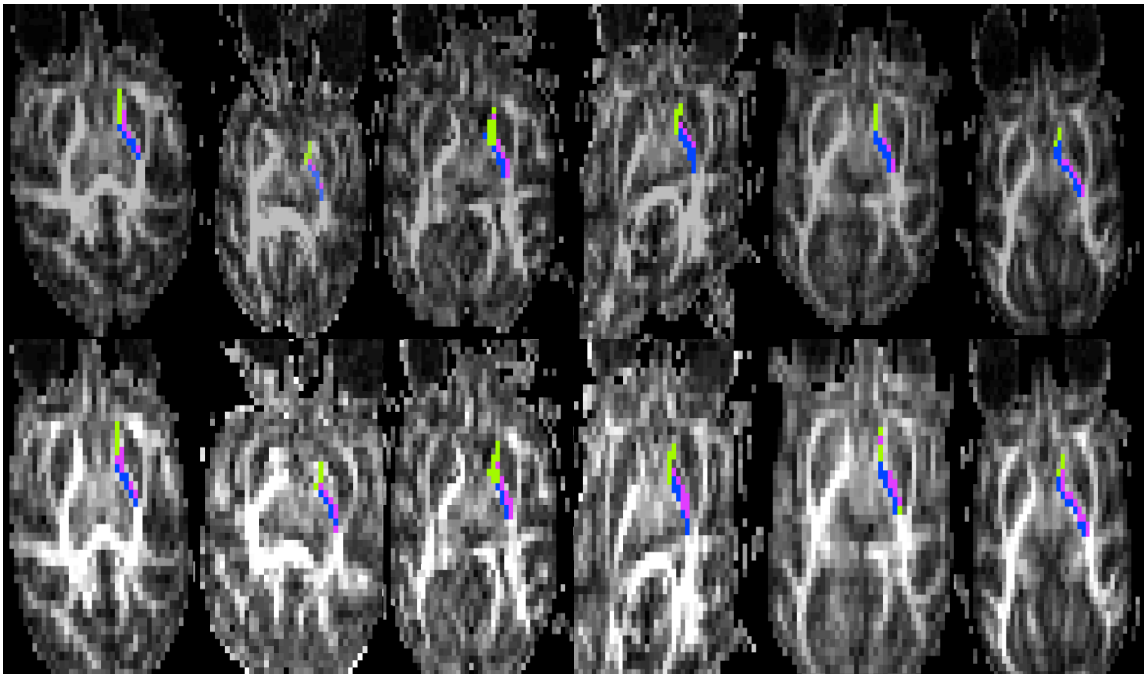

Figure 12. Impact of correction on hard segmentation across the 6 studies. Green regions had the highest probability of connection to caudate, purple and blue to LN and thalamus, respectively. The top row (A) shows segmentation before the correction. The bottom row (B) after correction. The patterns seem similar in top and bottom row, and although many voxels change classification it is not clear how the Morris correction impacted results.

CHAPTER IV

DISCUSSION AND CONCLUSION

We investigated anatomical connectivity of the internal capsule to three bordering subcortical structures (caudate, LN, and thalamus) with particular focus on the impact of a statistical correction to account for distance-related bias. In general, the correction shifts connectivity patterns away from one in which proximity determines the degree of connectivity. After the correction, the caudate is most strongly and consistently connected to the anterior limb of the IC with some connection to the posterior limb. The LN is most strongly and consistently connected to the lateral genu of the IC. The thalamus is most strongly and consistently connected to the medial genu of the IC.

Tracer studies provide support for the results. Leichnetz and Astruc found connections between the anterior limb of the IC and the caudate[51]. Yeteran and Pandya noted a similar result[52]. Morecraft et al. observed a medial-lateral division in the anterior IC where medial regions were more connected to caudate and lateral regions to LN[53]. These results agree with the caudate and LN connectivity maps and the hard segmentation results. Tanaka found some evidence that medial regions in the genu and posterior limb were connected to the thalamus[54]. However, these tracer studies primarily

focused on cortical-subcortical connections and only noted if tracts passed through the IC along the way from subcortical nuclei to the cortex. Existing tracer studies therefore do not provide a comprehensive picture of connectivity between subcortical nuclei and the IC.

This study complements recent tractography based studies of connectivity of the IC. Zarei et al. studied connectivity of cortical structures through the IC, showing connectivity largely consistent with anatomical tracer studies[48]. Sullivan et al. showed age-related changes of fractional anisotropy and diffusivity measures in IC segmented by cortical connections. In general, patterns of cortical connectivity of the IC show organization along the anterior-posterior direction[55]. However, we find a distinct pattern in the organization of connections to subcortical nuclei along the lateral-medial direction.

The individual connectivity profiles may be more useful for DBS presurgical planning than hard segmentation results. To illustrate, figure 13 compares corrected hard segmentation with connectivity profiles indicating connectivity between IC and each of the three subcortical nuclei of interest. Although hard segmentation classifies the indicated voxel as most highly connected to thalamus, connectivity to caudate is nearly as large. This region would therefore be a poor target if selective stimulation of a single nucleus is expected to provide optimum therapeutic benefit.

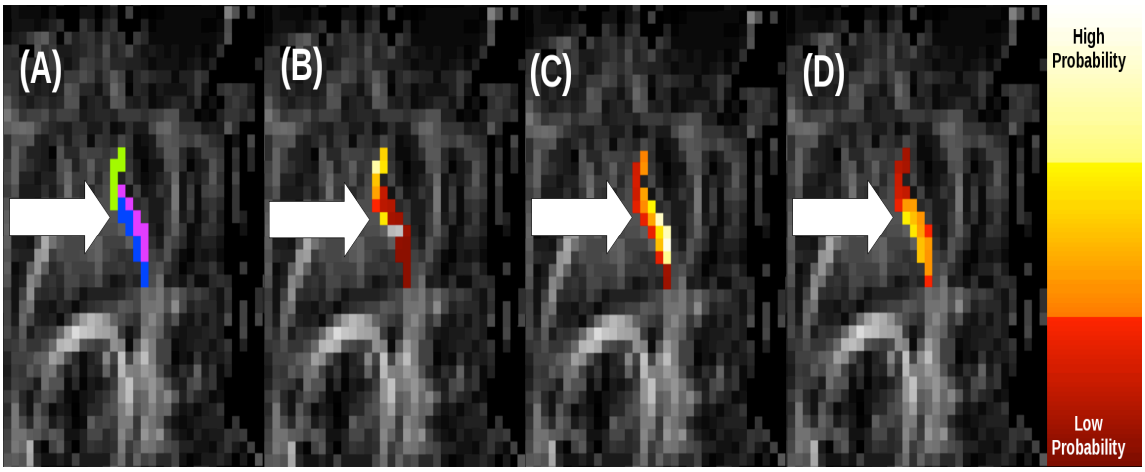

Figure 13. Comparison of hard segmentation (A) with connectivity profiles for caudate (B), LN (C) and thalamus (D). The arrow indicates a region most connected to thalamus, but which is also very highly connected to caudate.

This study was limited with regard to the ROIs. These limitations will be addressed in future studies. Although we followed the methodology of Zarei, et al., using FA maps to define ROIs[48], ROI selection is typically performed on high resolution anatomical images. However, HARDI images in this study covered only part of the brain in the inferior-superior direction as part of a trade-off between the need for high spatial resolution, adequate SNR, and memory limitations of the scanner. Unfortunately, we found it impossible to reliably coregister these partial-brain images with high resolution anatomical scans with standard techniques. Furthermore, distortions from the echo planar acquisition for the HARDI images typically result in the need for manual editing of ROIs using the FA maps after coregistration.

The inability to coregister to anatomical scans also prevented us from coregistering studies into a common space. Consequently, we were unable to generate average connectivity maps or quantify map consistency.

ROIs were determined manually, leading to systematic errors that can be addressed by automatic segmentation. Although there are widely used tools for automated segmentation of cortical structures, fewer tools exist for segmenting subcortical structures. Furthermore, these tools were optimized for human, not macaque, anatomy. As macaques are an important model for studies of the central nervous system, dedicated, automated methods for anatomical analysis of macaque images are an important need for the research community in general.

Although we follow others' precedents in using FA to identify regions[48], other diffusion-based contrasts can be used to identify regions. For example, generalized FA should improve contrast particularly in regions with crossing fibers and partial volume averaging[34].

A number of algorithms exist for tractography. Streamline tractography is commonly used[29], but probabilistic tractography is required to perform the Morris correction. Although we have demonstrated the use of the Morris correction using an in-house algorithm, the correction is completely compatible with publicly available tools such as FSL[56], Camino[57], and MRtrix[58]. Future work will evaluate the impact of the correction on different probabilistic tractography methodologies.

The definition of anatomical connectivity is an open question for the research community at large. One important methodological issue is partial volume averaging. As the subcortical regions are small, a relatively large layer of voxels at the border of each region is, in fact, a mixture of the tissue of interest and other tissue. A substantial fraction of tracks passing through these border voxels therefore do not truly intersect the tissue of interest, but neighboring tissue. The approach taken here simply assumes that if a track

intersects the user-defined ROI, it intersects the tissue of interest. The partial volume effect may be addressed by close examination of the trajectory of each track, excluding those that graze the edge of the tissue of interest. Future work will examine the extent of this effect on measured connectivity values.

The rejection sampling algorithm used to generate the tracks is simple, and further refinements may improve performance. Partial volume effects due to crossing fibers are accounted for by use of the FOD. However, beyond the relatively permissive 90 degree bending criterion, no further constraints were placed on track shapes. For example, tracks were not forbidden from looping back on themselves or re-entering the subcortical nuclei. Future work will examine appropriate constraints on track geometries for the assessment of anatomical connectivity.

An important distinction should be made regarding the nature of the Morris correction. The correction works on overall statistics of track counts, but not on the track geometries themselves. For example, the correction does not filter tracks with improbable *shapes* from a mixture of tracks with plausible and implausible trajectories. An alternative approach examining the statistics of shapes may be a valuable approach with better properties, but is beyond the scope of this paper.

Relatively little work has examined anatomical connectivity of subcortical structures by noninvasive means. The work of Iturria-Medina examined the connectivity patterns of a large number of brain regions, including subcortical regions[59,60]. An important issue to be examined is the degree to which the Morris correction would alter such patterns.

Future work will examine the efficacy of the Morris correction and subcortical

connections in detail. For example, simulations on digital phantoms can be used to quantitatively test the ability of the Morris correction to account for the distance-related falloff in anatomical connectivity. Such simulations can also be used to clarify distinctions in performance of the Morris correction in conjunction with different probabilistic tractography algorithms. Furthermore, consistency with ground-truth studies of connectivity using anatomical tracers are another indirect method for validating anatomical connectivity results[61]. This type of approach has been taken by Hagmann et al[62]

A number of opportunities for optimizing the methodology of measuring anatomical connectivity are available. Beyond the algorithmic approaches mentioned earlier in the discussion, details of the image acquisition such as spatial resolution, diffusion-weighting, and gradient acquisition scheme can each play an important role.

Optimization requires a reliable methodology for ground-truth validation. Beside simulations and comparison with known anatomical connectivity patterns in macaques, it may also be possible to use electrophysiology measurements taken in humans during DBS placement. There have been several recent clinical studies using tractography in surgical planning for DBS. Gutman, et al. analyzed the connectivity patterns of subcallosal cingulate and anterior limb of internal capsule, two common stimulation sites for depression[63]. Barkhoudarian, et al. looked at tractography results for three DBS patients suggesting that tractography could help clinicians characterize potential effects and side effects on a patient by patient basis[64]. Coenen, et al. used tractography to implicate the dentate-rubro-thalamic tract in controlling tremor in a single DBS patient[65]. None of these seem to have addressed the distance artifact.

DBS is attractive to study with tractography precisely because it provides some possibility of optimizing tractography parameters via cross-validation with interoperative electrophysiology and surgical outcomes. Modeling of stimulation patterns from implanted electrodes can be used to determine consistency between connectivity profiles and observed clinical outcomes and side effects[66]. Upon validation of the connectivity profiles, we hope to prospectively inform DBS implantation and stimulation parameters for improved clinical outcomes.

REFERENCES

1. Breit, S., Schulz, J.B. & Benabid, A.L. Deep brain stimulation. *Cell Tissue Res* **318**, 275-288 (2004).
2. Rodriguez-Oroz, M.C. et al. Bilateral deep brain stimulation in Parkinson's disease: a multicentre study with 4 years follow-up. *Brain* **128**, 2240 -2249 (2005).
3. Deuschl, G. et al. A Randomized Trial of Deep-Brain Stimulation for Parkinson's Disease. *New England Journal of Medicine* **355**, 896-908 (2006).
4. Machado, A. et al. Deep brain stimulation for Parkinson's disease: Surgical technique and perioperative management. *Mov. Disord.* **21**, S247-S258 (2006).
5. Ondo, W., Jankovic, J., Schwartz, K., Almaguer, M. & Simpson, R.K. Unilateral thalamic deep brain stimulation for refractory essential tremor and Parkinson's disease tremor. *Neurology* **51**, 1063 -1069 (1998).
6. Vercueil, L. et al. Deep brain stimulation in the treatment of severe dystonia. *Journal of Neurology* **248**, 695-700 (2001).
7. Loddenkemper, T. et al. Deep Brain Stimulation in Epilepsy. *Journal of Clinical Neurophysiology* **18**, (2001).
8. Mayberg, H.S. et al. Deep Brain Stimulation for Treatment-Resistant Depression. *Neuron* **45**, 651-660 (2005).
9. Greenberg, B.D. et al. Three-Year Outcomes in Deep Brain Stimulation for Highly Resistant Obsessive-Compulsive Disorder. *Neuropsychopharmacology* **31**, 2384-2393 (2006).
10. McIntyre, C.C., Savasta, M., Kerkerian-Le Goff, L. & Vitek, J.L. Uncovering the mechanism(s) of action of deep brain stimulation: activation, inhibition, or both.

Clinical Neurophysiology **115**, 1239-1248 (2004).

11. Frankemolle, A.M.M. et al. Reversing cognitive–motor impairments in Parkinson's disease patients using a computational modelling approach to deep brain stimulation programming. *Brain* **133**, 746 -761 (2010).
12. biomed.brown.edu/Courses/BI108/BI108_2008_Groups/group07/Parkinsons.html Last accessed on June 26, 2011.
13. McIntyre, C.C. & Hahn, P.J. Network perspectives on the mechanisms of deep brain stimulation. *Neurobiology of Disease* **38**, 329-337 (2010).
14. Johnson, M.D., Miocinovic, S., McIntyre, C.C. & Vitek, J.L. Mechanisms and Targets of Deep Brain Stimulation in Movement Disorders. *Neurotherapeutics* **5**, 294-308 (2008).
15. McIntyre, C. Electric field and stimulating influence generated by deep brain stimulation of the subthalamic nucleus. *Clinical Neurophysiology* **115**, 589-595 (2004).
16. Butson, C.R. & McIntyre, C.C. Role of electrode design on the volume of tissue activated during deep brain stimulation. *J. Neural Eng.* **3**, 1-8 (2006).
17. Butson, C.R., Cooper, S.E., Henderson, J.M. & McIntyre, C.C. Patient-specific analysis of the volume of tissue activated during deep brain stimulation. *NeuroImage* **34**, 661-670 (2007).
18. Behrens, T.E.J. et al. Non-invasive mapping of connections between human thalamus and cortex using diffusion imaging. *Nat Neurosci* **6**, 750-757 (2003).
19. Jones, D.K. Studying connections in the living human brain with diffusion MRI. *Cortex* **44**, 936-952 (2008).

20. Skudlarski, P. et al. Measuring brain connectivity: Diffusion tensor imaging validates resting state temporal correlations. *NeuroImage* **43**, 554-561 (2008).
21. Moseley, M.E., Kucharczyk, J., Asgari, H.S. & Norman, D. Anisotropy in diffusion-weighted MRI. *Magnetic Resonance in Medicine* **19**, 321-326 (1991).
22. Einstein, A. Über die von der molekularkinetischen Theorie der Wärme geforderte Bewegung von in ruhenden Flüssigkeiten suspendierten Teilchen. *Annalen der Physik* **322**, 549-560 (1905).
23. Torrey, H.C. Bloch Equations with Diffusion Terms. *Phys. Rev.* **104**, 563 (1956).
24. Stejskal, E.O. & Tanner, J.E. Spin Diffusion Measurements: Spin Echoes in the Presence of a Time-Dependent Field Gradient. *J. Chem. Phys.* **42**, 288 (1965).
25. Mori, S. & Barker, P.B. Diffusion magnetic resonance imaging: Its principle and applications. *The Anatomical Record* **257**, 102-109 (1999).
26. Basser, P.J., Mattiello, J. & LeBihan, D. MR diffusion tensor spectroscopy and imaging. *Biophysical Journal* **66**, 259-267 (1994).
27. Basser, P.J., Mattiello, J. & Lebihan, D. Estimation of the Effective Self-Diffusion Tensor from the NMR Spin Echo. *Journal of Magnetic Resonance, Series B* **103**, 247-254 (1994).
28. Westin, C.-F. et al. Processing and visualization for diffusion tensor MRI. *Med Image Anal* **6**, 93-108 (2002).
29. Mori, S., Crain, B.J., Chacko, V.P. & Van Zijl, P.C.M. Three-dimensional tracking of axonal projections in the brain by magnetic resonance imaging. *Annals of Neurology* **45**, 265-269 (1999).
30. Basser, P.J., Pajevic, S., Pierpaoli, C., Duda, J. & Aldroubi, A. In vivo fiber

tractography using DT-MRI data. *Magnetic Resonance in Medicine* **44**, 625-632 (2000).

31. Conturo, T.E. et al. Tracking neuronal fiber pathways in the living human brain. *Proceedings of the National Academy of Sciences* **96**, 10422 -10427 (1999).
32. Tuch, D.S. et al. High angular resolution diffusion imaging reveals intravoxel white matter fiber heterogeneity. *Magn. Reson. Med.* **48**, 577-582 (2002).
33. Behrens, T.E.J., Berg, H.J., Jbabdi, S., Rushworth, M.F.S. & Woolrich, M.W. Probabilistic diffusion tractography with multiple fibre orientations: What can we gain? *NeuroImage* **34**, 144-155 (2007).
34. Tuch, D.S. Q-ball imaging. *Magn Reson Med* **52**, 1358-1372 (2004).
35. Wedeen, V.J. et al. Diffusion spectrum magnetic resonance imaging (DSI) tractography of crossing fibers. *NeuroImage* **41**, 1267-1277 (2008).
36. Parker, G.J.M. & Alexander, D.C. Probabilistic anatomical connectivity derived from the microscopic persistent angular structure of cerebral tissue. *Philosophical Transactions of the Royal Society B: Biological Sciences* **360**, 893 -902 (2005).
37. Behrens, T.E.J. et al. Characterization and propagation of uncertainty in diffusion-weighted MR imaging. *Magnetic Resonance in Medicine* **50**, 1077-1088 (2003).
38. Yamada, K. Diffusion tensor tractography should be used with caution. *Proceedings of the National Academy of Sciences* **106**, E14 (2009).
39. Morris, D.M., Embleton, K.V. & Parker, G.J.M. Probabilistic fibre tracking: Differentiation of connections from chance events. *NeuroImage* **42**, 1329-1339 (2008).

40. Haber, S.N. The primate basal ganglia: parallel and integrative networks. *Journal of Chemical Neuroanatomy* **26**, 317-330 (2003).
41. Haber, S.N. & Brucker, J.L. Cognitive and limbic circuits that are affected by deep brain stimulation. *Frontiers in Bioscience* **14**, 1823-1834 (2009).
42. Xu, W. et al. Dissociation of motor symptoms during deep brain stimulation of the subthalamic nucleus in the region of the internal capsule. *Experimental Neurology* **In Press, Uncorrected Proof**, (2010).
43. Gray, H. *Anatomy of the Human Body*. (Lea & Febiger: Philadelphia, 1918).
44. Basser, P.J. & Pierpaoli, C. Microstructural and Physiological Features of Tissues Elucidated by Quantitative-Diffusion-Tensor MRI. *Journal of Magnetic Resonance, Series B* **111**, 209-219 (1996).
45. Tournier, J.-D., Calamante, F., Gadian, D.G. & Connelly, A. Direct estimation of the fiber orientation density function from diffusion-weighted MRI data using spherical deconvolution. *NeuroImage* **23**, 1176-1185 (2004).
46. Sakaie, K.E. & Lowe, M.J. An objective method for regularization of fiber orientation distributions derived from diffusion-weighted MRI. *NeuroImage* **34**, 169-176 (2007).
47. Saleem, K.S. & Logothetis, N.K. *A combined MRI and histology atlas of the rhesus monkey brain in stereotaxic coordinates*. (Academic Press: 2006).
48. Zarei, M. et al. Two-dimensional population map of cortical connections in the human internal capsule. *J. Magn. Reson. Imaging* **25**, 48-54 (2007).
49. Lowe, M.J. et al. Resting state sensorimotor functional connectivity in multiple sclerosis inversely correlates with transcallosal motor pathway transverse diffusivity.

Hum. Brain Mapp. **29**, 818-827 (2008).

50. Smith, S.M. Fast robust automated brain extraction. *Hum. Brain Mapp.* **17**, 143-155 (2002).
51. Leichnetz, G.R. & Astruc, J. The efferent projections of the medial prefrontal cortex in the squirrel monkey (Saimiri sciureus). *Brain Research* **109**, 455-472 (1976).
52. Yeterian, E.H. & Pandya, D.N. Prefrontostriatal connections in relation to cortical architectonic organization in rhesus monkeys. *J. Comp. Neurol.* **312**, 43-67 (1991).
53. Morecraft, R.J. et al. Localization of arm representation in the corona radiata and internal capsule in the non-human primate. *Brain* **125**, 176 -198 (2002).
54. Tanaka, J. Thalamic projections of the dorsomedial prefrontal cortex in the rhesus monkey (Macaca mulatta). *Brain Research* **110**, 21-38 (1976).
55. Sullivan, E.V., Zahr, N.M., Rohlfing, T. & Pfefferbaum, A. Fiber tracking functionally distinct components of the internal capsule. *Neuropsychologia* **48**, 4155-4163 (2010).
56. Smith, S.M. et al. Advances in functional and structural MR image analysis and implementation as FSL. *NeuroImage* **23**, S208-S219 (2004).
57. Cook, P.A. et al. Camino: Open-Source Diffusion-MRI Reconstruction and Processing. *14th Scientific Meeting of the International Society for Magnetic Resonance in Medicine* 2759 (2006).
58. Tournier, J.-D., Calamante, F., Gadian, D.G. & Connelly, A. Probabilistic fibre tracking through regions containing crossing fibres. *13th Annual Meeting of ISMRM* 1343 (2005).
59. Iturria-Medina, Y. et al. Characterizing brain anatomical connections using diffusion

weighted MRI and graph theory. *NeuroImage* **36**, 645-660 (2007).

60. Iturria-Medina, Y., Sotero, R.C., Canales-Rodríguez, E.J., Alemán-Gómez, Y. & Melie-García, L. Studying the human brain anatomical network via diffusion-weighted MRI and Graph Theory. *NeuroImage* **40**, 1064-1076 (2008).
61. Modha, D.S. & Singh, R. Network architecture of the long-distance pathways in the macaque brain. *Proceedings of the National Academy of Sciences* **107**, 13485 -13490 (2010).
62. Hagmann, P. et al. Quantitative validation of MR tractography using the CoCoMac database. *16th Annual Meeting of ISMRM* 427 (2008).at <http://www.ismrm.org/06/2006_program.htm>
63. Gutman, D.A., Holtzheimer, P.E., Behrens, T.E.J., Johansen-Berg, H. & Mayberg, H.S. A Tractography Analysis of Two Deep Brain Stimulation White Matter Targets for Depression. *Biological Psychiatry* **65**, 276-282 (2009).
64. Barkhoudarian, G. et al. A role of diffusion tensor imaging in movement disorder surgery. *Acta Neurochirurgica* **152**, 2089-2095 (2010).
65. Coenen, V.A., Mädler, B., Schiffbauer, H., Urbach, H. & Allert, N. Individual Fiber Anatomy of the Subthalamic Region Revealed With Diffusion Tensor Imaging: A Concept to Identify the Deep Brain Stimulation Target for Tremor Suppression. *Neurosurgery* **68**, (2011).
66. Miocinovic, S. et al. Experimental and theoretical characterization of the voltage distribution generated by deep brain stimulation. *Experimental Neurology* **216**, 166-176 (2009).